Storage of 1000 holograms with use of a dual-wavelength method

Ernest Chuang and Demetri Psaltis

We demonstrate the storage of 1000 holograms in a memory architecture that makes use of different wavelengths for recording and readout to reduce the grating decay while retrieving data. Bragg-mismatch problems from the use of two wavelengths are minimized through recording in the image plane and using thin crystals. Peristrophic multiplexing can be combined with angle multiplexing to counter the poorer angular selectivity of thin crystals. Dark conductivity reduces the effectiveness of the dual-wavelength method for nonvolatile readout, and constraints on the usable pixel sizes limit this method to moderate storage densities. © 1997 Optical Society of America

Key words: Volume holographic memory, dual-wavelength method, nonvolatile readout, peristrophic multiplexing, exposure schedule.

1. Introduction

When a photorefractive crystal is used as the recording material in a holographic memory, the recorded gratings decay when illuminated by the readout beam. Several methods have been developed to address this problem.[1–10] We use the dual-wavelength method[8–10] to demonstrate experimentally the long-term storage of 1000 holograms. The motivation for using different wavelengths of light for recording and readout is simple: If a crystal has an absorption spectrum with a substantial variation as a function of wavelength, by recording at a wavelength λ_1 at which the crystal is highly sensitive and reading out at a second wavelength λ_2 at which the crystal is relatively insensitive, we can reduce the decay of the gratings caused by the readout illumination.

Implementing the dual-wavelength method is straightforward for a single grating. Figure 1 shows the dual-wavelength configuration for the transmission geometry, along with the corresponding k-space diagram. Similar diagrams can be drawn readily for the reflection and 90° geometries also. A grating is recorded in the usual manner, with signal and reference beams at the first wavelength λ_1. We recon-

struct this grating at the second wavelength λ_2 by introducing the readout beam at an angle tilted with respect to the recording reference beam. We assume that the wave vectors of all the beams lie in the horizontal (x–z) plane. Bragg-matched readout occurs when the readout beam is positioned such that the grating vector lies at the intersection of the two k spheres. The condition necessary for achieving Bragg-matched readout must satisfy the following relationships[10]:

$$\frac{\sin\left[\frac{1}{2}(\phi_r + \phi_s)\right]}{\lambda_2} = \frac{\sin\left[\frac{1}{2}(\theta_r + \theta_s)\right]}{\lambda_1},\qquad(1)$$

$$\phi_r - \phi_s = \theta_r - \theta_s.$$

In the above, θ_r and θ_s are the reference- and the signal-beam angles, respectively, at λ_1; and ϕ_r and ϕ_s are the reference- and the diffracted signal-beam angles at λ_2. All angles and wavelengths are defined inside the crystal, with angles measured with respect to the z axis (the normal to the crystal face).

Although we can easily Bragg match a single grating, when a hologram of an image that consists of many plane-wave components is recorded, it is generally impossible to match the entire spectrum simultaneously with a single plane-wave readout reference. We show that, by use of a sufficiently thin crystal and the peristrophic multiplexing technique,[11] a large number of holograms can be stored and recalled with a single plane-wave reference.

The authors are with the Department of Electrical Engineering, Mail Stop 136-93, California Institute of Technology, Pasadena, California 91125.

Received 10 February 1997; revised manuscript received 16 May 1997.

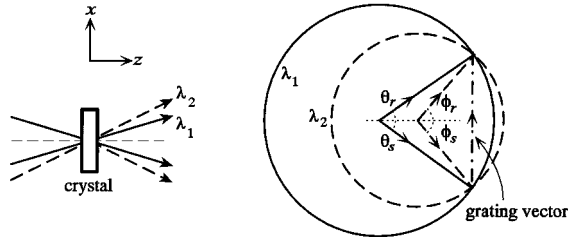0003-6935/97/328445-10$10.00/0
© 1997 Optical Society of America

Fig. 1. Dual-wavelength scheme in transmission geometry with the corresponding k-space diagram for Bragg matching a single grating.

2. Dual-Wavelength Readout of Complex Signal

Recording an image that consists of many plane-wave components can be represented in k space by a cone of signal vectors that interferes with the reference beam to record a cone of grating vectors, as shown in Fig. 2. When we attempt to reconstruct the signal with a reference at λ_2, only the gratings that lie on the circle of intersection between the two k spheres are exactly Bragg matched. Hence only an arc of the signal cone is strongly reconstructed.

The diffracted intensity I_{diff} of the hologram reconstruction at λ_2 is given by

$$I_{\text{diff}} \sim \text{sinc}^2\left(\frac{L}{2\pi}\Delta k_z\right), \qquad (2)$$

where L is the crystal thickness and Δk_z is the parameter that determines the degree of Bragg mismatch. For a plane-wave component in the signal
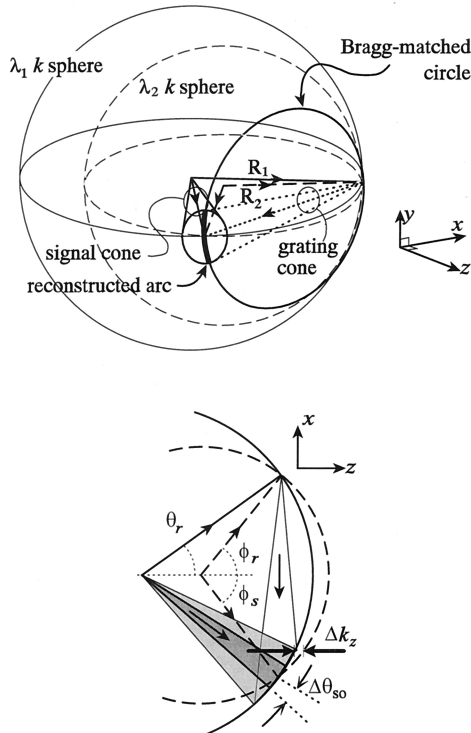
beam whose k vector lies in the x–z plane and is offset from the central zero-order component by $\Delta\theta_s$, the Bragg mismatch Δk_z is given by

$$\Delta k_z = 2\pi\left(\frac{\cos\phi_r}{\lambda_2} + \frac{\cos(\theta_s + \Delta\theta_s) - \cos(\theta_r)}{\lambda_1} - \left\{\left(\frac{1}{\lambda_2}\right)^2\right. \right.$$
$$\left.\left. - \left[\frac{\sin\phi_r}{\lambda_2} - \frac{\sin\theta_r + \sin(\theta_s + \Delta\theta_s)}{\lambda_1}\right]^2\right\}^{1/2}\right). \qquad (3)$$

If $\Delta\theta_s = 0$ and Eq. (1) is satisfied, then $\Delta k_z = 0$ and I_{diff} is maximum. As $\Delta\theta_s$ increases, the diffracted power decreases.

For simplicity let us consider the range of reconstructed signal components to be those that lie within the main lobe of the sinc envelope function. In practice the range will be slightly narrower because there will be some minimum detectable intensity threshold that limits us before we reach the first null. There will also be faintly reconstructed sidelobes outside the main lobe. We neglect variations normal to the plane of interaction between the signal and the reference beams (the y direction in Fig. 2), i.e., we approximate the reconstructed arc to be a straight line, which is reasonable for signal cones with small angular bandwidths. Equating Δk_z to $2\pi/L$ and solving for $\Delta\theta_s$ yields the angular location of the first null of expression (2) within the signal cone. If we make the approximation that $\lambda_1, \lambda_2 \ll L$ (which is almost always true for the wavelengths and the crystals that we use in practice), then the angular bandwidth of the main lobe of the sinc function can be approximated by

$$\sin\Delta\theta_{so} = \frac{\lambda_1\cos\phi_s}{L\sin(\phi_r - \theta_r)}, \qquad (4)$$

where $\Delta\theta_{so}$ is the usable bandwidth of the signal cone in the x–z plane. Note that ϕ_s and ϕ_r are not independent variables; they are both determined by the recording beam angles θ_s and θ_r and the wavelengths λ_1 and λ_2, as shown in Eq. (1). Also note that after we select λ_1 and λ_2 we can still make the signal bandwidth arbitrarily high by decreasing L. Therefore there is a trade-off between the usable signal bandwidth and the number of holograms that can be angularly multiplexed at one location.

3. Reconstruction Effects

The effect on the reconstructed image of limiting the bandwidth of the signal cone depends on whether we record in the Fourier plane or the image plane. We first consider the case of recording in the Fourier plane [Fig. 3(a)]. When we record in the Fourier plane, each plane-wave component of the signal beam that enters the crystal corresponds to a spatial location (pixel) on the input image. Hence, if we reconstruct only a limited angular bandwidth $\Delta\theta_{so}$ of the signal cone in the x dimension, we expect to reconstruct a strip of the image, limited in the x dimension. An example of such a reconstruction is shown in Fig. 3(b) for $\lambda_1' = 488$ nm, $\lambda_2' = 633$ nm (wavelengths in
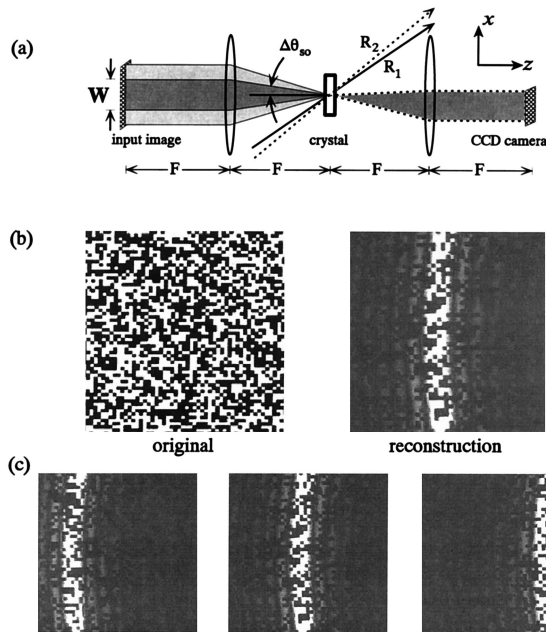

Fig. 2. k-sphere diagram for the dual-wavelength transmission geometry with a complex signal (assumes $\lambda_2 > \lambda_1$).

Fig. 3. Fourier-plane recording: (a) system setup, (b) comparison of input image and reconstruction at λ_2, (c) reconstructions with three slightly detuned angles of the λ_2 reference beam R_2.

Fig. 4. Image-plane recording: (a) system setup and (b) comparison of input image and reconstruction at λ_2.

air), and $L = 4.6$ mm. In the figure we see a slight arc in the reconstruction resulting from the Bragg mismatch in the y dimension as well as side lobes from the sinc modulation in the x dimension. The curvature that is observed experimentally is due to the fact that the intersection of the two k spheres in Fig. 2 is a circle, and a small arc of this circle is spanned by the signal cone. This effect was neglected in the derivation of Eqs. (3) and (4).

From the system geometry, we can derive the width W of the reconstructed image strip:

$$W = \frac{2Fn \, \sin \Delta\theta_{so}}{(1 - n^2 \, \sin^2 \Delta\theta_{so})^{1/2}}, \qquad (5)$$

where F is the focal length of the Fourier transforming lens and n is the refractive index of the material at λ_1. We assume the crystal to be in air and the central component of the signal beam to be on axis. For signals tilted from the crystal normal, Eq. (5) must be adjusted for variations resulting from the Snell law. In Fig. 3(c) we show how the entire image can be sequentially scanned by changing the angle of the readout reference to reveal different portions or strips of the stored image.

Recording in the image plane [Fig. 4(a)] is analagous to recording in the Fourier plane except that in place of the input image we would have its Fourier transform. Therefore, instead of reconstructing a strip of the image, we reconstruct a strip or band of the frequency spectrum of the image. If we position the readout reference to Bragg-match the zero-order component of the image, the resulting reconstruction will be a low-pass-filtered version of the original in the x dimension. Figure 4(b) compares the recon-
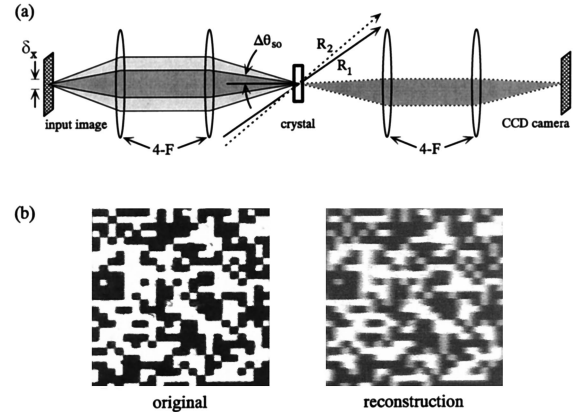
struction at $\lambda_2' = 633$ nm to that obtained by the original ($\lambda_1' = 488$ nm) reference. Note the blurring of the edges in the x dimension that results from the loss of the high-frequency components of the input signal. The angular spread α owing to the aperture of a pixel of width δ_x is

$$\sin \alpha = \frac{\lambda}{\delta_x}. \qquad (6)$$

We equate α to $\Delta\theta_{so}$ in Eq. (4) and solve for δ_x to obtain a rough estimate for the minimum pixel width $\delta_{x,\min}$ that can be reconstructed by the second wavelength,

$$\delta_{x,\min} = \frac{L \, \sin(\phi_r - \theta_r)}{\cos \phi_s}. \qquad (7)$$

In a manner similar to the Fourier case, we can also scan the reference beam to bandpass different frequency components of the original image.

A number of solutions have been proposed for the Bragg-mismatch problem of the dual-wavelength scheme. Most have dealt with Fourier-plane recording, such as the use of spherical readout beams[8] to Bragg-match a larger range of the signal cone or interleaving strips from adjacent holograms.[10] We can also recover all the necessary information by recording in the image plane, without the added complexity of the above methods, if we simply adjust the system parameters according to the resolution of the images that we wish to store.

From Eq. (4) we see that we can maximize $\Delta\theta_{so}$ by

• reducing the crystal thickness L,
• using wavelengths λ_1 and λ_2 that are as close together as possible, or
• reducing the angle between the signal and the reference beams.

Figure 5(a) shows a reconstruction of a random pixel pattern with four regions of different pixel sizes, from 50 to 200 μm^2, recorded in a crystal of thickness $L = 4.6$ mm. The recording parameters were $\lambda_1' =$
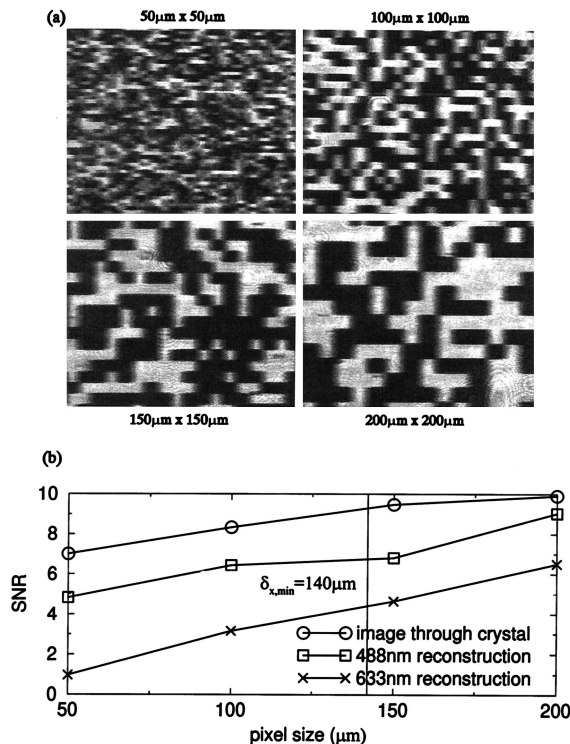
Fig. 5. (a) Reconstruction of data mask with pixel sizes varying from 50 to 200 μm^2, recorded in a 4.6-mm-thick crystal, recorded with $\lambda_1' = 488$ nm and read with $\lambda_2' = 633$ nm. (b) Plot of SNR versus pixel size from the image in (a) compared with SNR measured from the data mask imaged through the crystal and when reconstructed with the original λ_1 reference (images not shown).

488 nm, $\lambda_2' = 633$ nm, $\theta_s = 0°$, and $\theta_r = 11.6°$, which correspond to a theoretical minimum acceptable pixel size of $\delta_{x,min} \approx 140$ μm. From the figure we see that, although there is always the edge blurring in the x direction, we can still easily distinguish between ON and OFF pixels for the 150- and 200-μm pixels, but we get a progressive loss of detail for smaller pixel sizes. Figure 5(b) shows how the signal-to-noise ratio (SNR) of the images varies with pixel size. Here we defined SNR as

$$SNR = \frac{\mu_1 - \mu_0}{(\sigma_1{}^2 + \sigma_0{}^2)^{1/2}}, \quad (8)$$

where $\mu_{1,0}$ and $\sigma_{1,0}{}^2$ are the mean and the variances of the ON (1) and the OFF (0) pixels. Depending on the application, we can choose the pixel size to achieve the desired SNR.

Figure 6 shows two image-plane reconstructions of the same pattern—one recorded in a 4.6-mm-thick crystal and another in a 0.25-mm-thick crystal. Using the same recording geometry we used for Fig. 5, we compared $\delta_{x,min}$ for the thinner crystal at 7.6 μm with 140 μm for the thicker crystal. This is evident in Fig. 6, where the reconstruction from the thinner crystal preserves the higher spatial frequencies so that the edge blurring is hardly noticeable. Rectangular pixels were used for these images for demonstrating that the pixel-size limitation is only in the x
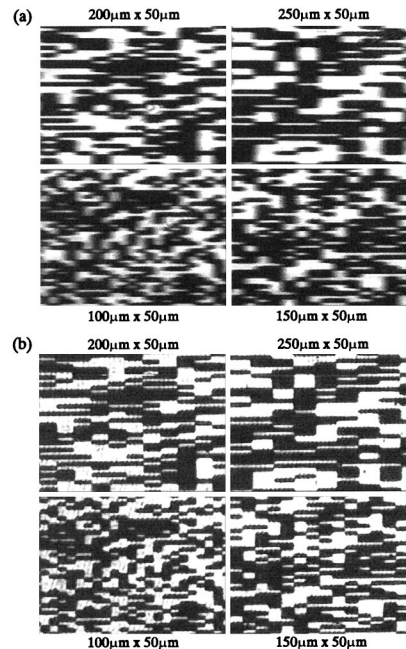
Fig. 6. (a) Reconstruction of data mask with pixel widths varying from 100 to 250 μm, recorded in a 4.6-mm-thick crystal. (b) Same image reconstructed from a recording in a 250-μm-thick crystal.

dimension; even the thicker crystal reconstructs high spatial frequencies cleanly in the y dimension.

The main problem that results from the use of thinner crystals is a loss in the angular selectivity. The first null of the angular selectivity function is given by[12]

$$\Delta\phi = \frac{\lambda_2'}{L} \frac{\cos \phi_s}{\sin(\phi_r + \phi_s)}, \quad (9)$$

where $\Delta\phi$ is the angle outside the crystal by which we must rotate the reference beam (or, alternatively, rotate the crystal) to reach the first null. λ_2' is the readout wavelength outside the crystal, and ϕ_s and ϕ_r are the beam angles inside the crystal. Because the selectivity is inversely proportional to the crystal thickness L, changing to a thinner crystal reduces the number of angular locations at which we can store holograms.

We can store a large number of holograms in a thin medium by using peristrophic multiplexing[11] in addition to angle multiplexing. For peristrophic multiplexing we rotate the crystal about the normal to its surface. This causes the reconstructions from adjacent holograms to be separated spatially at the Fourier plane so that we may selectively pass a single hologram by placing an aperture at this plane. The peristrophic selectivity for image-plane recording is given by

$$\Delta\psi = \frac{2\lambda_2}{\delta_y(\sin \phi_s + \sin \phi_r)}, \quad (10)$$

where $\Delta\psi$ is the angle by which we must rotate the crystal around its normal between peristrophic loca-
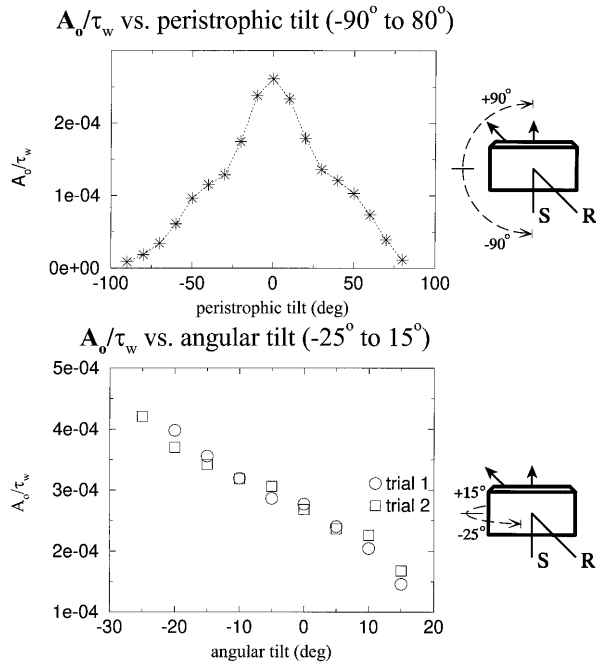
A_o/τ_w vs. peristrophic tilt (-90° to 80°)

A_o/τ_w vs. angular tilt (-25° to 15°)

Fig. 7. Variation of recording slope (A_o/τ_w) with peristrophic and angular crystal tilts.

Fig. 8. System setup used for the dual-wavelength experiments.

tions, and δ_y is the pixel size in the y dimension. What is important to note from this equation is that this selectivity is insensitive to the crystal thickness L. Therefore, while we suffer in angular selectivity by using thinner crystals, the peristrophic selectivity remains unchanged.

It is unfortunate that peristrophic multiplexing introduces a new problem of its own. Unlike photopolymers, with which peristrophic multiplexing was originally demonstrated, the recording behavior of photorefractive crystals depends on the orientation of the crystal with respect to the gratings being written. Therefore, as we rotate the beams or the crystal, the recording efficiency of each location will be different. A related problem is the possibility of observing double gratings[13] if the polarizations of the recording and/or readout beams are not maintained in alignment with the ordinary or extraordinary axis of the crystal as the crystal is rotated peristrophically. This could be done with circularly polarized beams and polarizers attached in front of the crystal; however, for small peristrophic rotations it is sufficient to use fixed polarizations relative to the plane of interaction. No secondary reconstructions were observed experimentally for peristrophic rotations of less than 10°.

Figure 7 shows experimental plots of the writing slope (the time derivative of the square root of diffraction efficiency during recording, A_o/τ_w) versus crystal rotation for peristrophic and angular tilts of the crystal in the image-plane geometry setup shown in Fig. 8. As expected, the recording efficiency drops off quickly as the c axis of the crystal is rotated away from the direction of the grating during peristrophic rotation. The variation with angular tilt does not
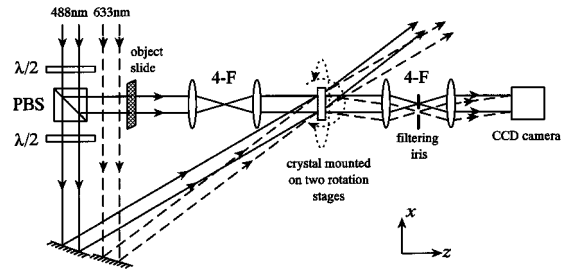
peak when the signal and the reference beams are symmetrically oriented around the crystal normal as might be expected. This asymmetry is due to additional contributing factors such as variations in Fresnel reflections and changes in the shape of the hologram interaction region inside the crystal as the crystal is tilted in angle.

The conventional exposure schedule[14] for recording multiple holograms with equal diffraction efficiencies assumes that all holograms record at the same rate and are characterized by a uniform writing slope A_o/τ_w. Because A_o/τ_w varies with the recording position in our case, we must derive a new schedule that compensates for the variation in recording behavior. We model the recording and erasure behavior as shown in Fig. 9. Each hologram is assumed to have a unique writing slope $(A_o/\tau_w)_m$, where m is the hologram number; but all holograms are assumed to share a common erasure time constant τ_e. If all holograms decay at the same rate, for maintaining uniform final diffraction efficiencies, we must only ensure that each new hologram is written to the point that its grating strength equals that of the previously written holograms as they decay. We can write this requirement as

$$A_m = A_{m+1},$$

$$A_{o,m}[1 - \exp(-t_m/\tau_{w,m})]\exp(-t_{m+1}/\tau_e)$$
$$= A_{o,m+1}[1 - \exp(-t_{m+1}/\tau_{w,m+1})], \quad (11)$$

where, for the mth hologram, A_m is the grating amplitude, $A_{o,m}$ is the grating amplitude at saturation,
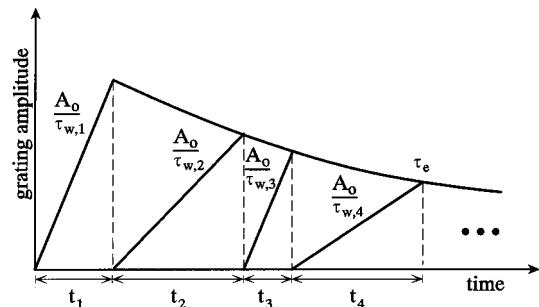

Fig. 9. Model for determining the compensated exposure schedule; it allows variation in the recording rate at each location but assumes that all holograms share a common decay rate.

$\tau_{w,m}$ is the writing-time constant, and t_m is the exposure time. Solving for t_m we obtain

$$t_m = -\tau_{w,m} \ln\left\{1 - \frac{A_{o,m+1}}{A_{o,m}} \exp(t_{m+1}/\tau_e)\right.$$

$$\left. \times [1 - \exp(-t_{m+1}/\tau_{w,m+1})]\right\}, \qquad (12)$$

which gives us an iterative formula for calculating all the recording times, given an exposure time for the last hologram and knowing all the writing time constants and grating saturation amplitudes.

If we make the approximation that $t_m \ll \tau_{w,m}$, this simplifies to

$$t_m = \frac{(A_o/\tau_w)_{m+1}}{(A_o/\tau_w)_m} t_{m+1} \exp(t_{m+1}/\tau_e), \qquad (13)$$

for which we need to know only the relative magnitudes of the writing slopes, which we can obtain from the plots of recording slope versus crystal position in Fig. 7. Eq. (13) differs from the conventional schedule by the ratio of writing slopes. It can be shown that it is slightly better to record the holograms in the order of decreasing A_o/τ_w, but the difference is marginal.

4. Experiment

Figure 8 shows the experimental setup used for the dual-wavelength image-plane architecture. It consists of two $4f$ systems to image the input object through the crystal and onto the CCD detector, with two separate beam paths for the recording and the readout reference arms. We used $\lambda_1' = 488$ nm polarized out of plane for recording and $\lambda_2' = 633$ nm polarized in plane for readout, provided by an argon ion and a He–Ne laser, respectively. The photorefractive crystal was a LiNbO$_3$:Fe (0.015%) crystal, 4.6 mm thick, cut from a boule obtained from Crystal Technology, Inc., Palo Alto, Calif. The crystal was mounted on two rotation stages: One provided the angular tilt and the other the peristrophic tilt. The angle between the recording signal and the reference beams outside the crystal was 28.3°. The signal beam was on axis and the crystal c axis was in the x–z plane. The origin around which the angular and peristrophic rotations were referenced was where the crystal was positioned such that the c axis coincided with the x axis.

The measured angular selectivity for this geometry was $\Delta\phi = 0.035°$ for the first null with the 633-nm reference. In the experiment we used angular offsets of 0.2° to space the holograms past the fifth null to minimize cross talk. The theoretical peristrophic selectivity from Eq. (10) was $\Delta\psi = 0.79°$, whereas in practice we used peristrophic spacings of 2° to avoid cross talk from the sidelobes of the Fourier transform. Using 50 angular locations (from −4.9° to +4.9° tilt) and 20 peristrophic locations (from −9° to +9° and 171° to 189°), we recorded 1000 holograms with a 150-µm-pixel random bit pattern mask as input.
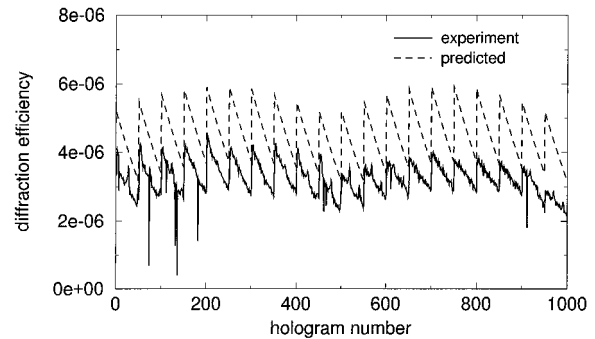
Fig. 10. Experimental and predicted distributions for the diffraction efficiencies of 1000 holograms when recorded with the conventional exposure schedule.

Using a conventional exposure schedule, we get a comb function of diffraction efficiency for the 1000 holograms, as shown in Fig. 10. Each sawtooth in the comb function corresponds to an angular sweep from −4.9° to +4.9° at a single peristrophic location. The slower variation is due to the peristrophic rotation. Also shown in the figure is the predicted comb function based on the recording slope variations from Fig. 7, where we extrapolated recording slopes for intermediate combinations of peristrophic and angular tilts from the two plots. The amplitude mismatch between the curves is simply due to the fact that the recording slopes used in the prediction were measured under different experimental parameters. Figure 11 shows the resulting comb function after the application of the compensated exposure schedule. The diffraction efficiencies are considerably more uniform at approximately 6×10^{-6}.

Of the 1000 holograms, we visually inspected approximately 100 for uniformity, and we randomly chose five for SNR and probability-of-error analysis. Figure 12(a) shows the original input image as seen through the crystal, a sample reconstruction at 488 nm, and two reconstructions at 633 nm. For hologram 263, we also show histograms for the 488- and 633-nm reconstructions in Fig. 12(b).

We measured the SNR by averaging CCD pixel values within each image pixel (each image pixel corresponded to approximately 13×12 CCD pixels) and
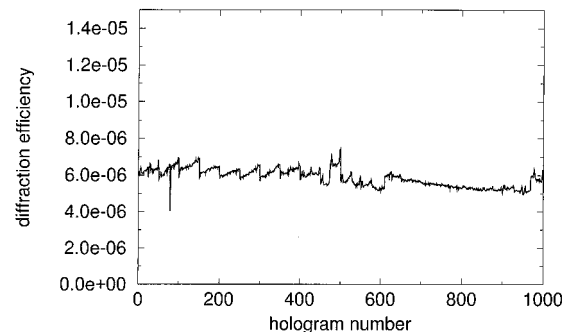

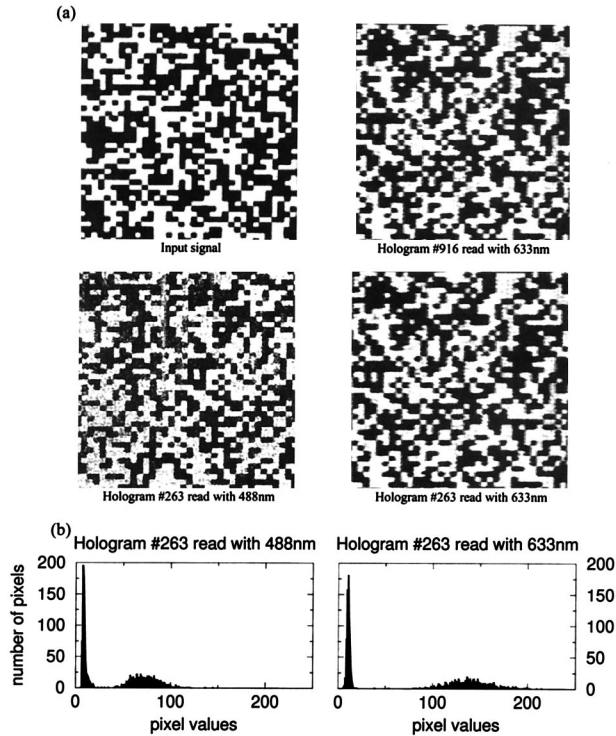Fig. 11. Diffraction efficiencies for 1000 holograms recorded with the compensated exposure schedule.

Fig. 12. (a) Sample images from 1000-hologram experiment with (b) corresponding histograms for λ_1 and λ_2 reconstructions.

Fig. 13. (a) Absorption spectrum and (b) decay curves for the LiNbO$_3$:Fe crystal.

then determining the SNR as given in Eq. (8). Probability of error was calculated, assuming χ^2 distributions to the histograms. For the reconstructions that were read out with the original reference at 488 nm, the SNR ranged from approximately 3.0 to 4.0, with corresponding probabilities of error from 10^{-4} to 10^{-5}. The results for the reconstructions at 633 nm were better than those at 488 nm despite the low-pass-filtering effect of the dual-wavelength image-plane readout. For the 633-nm reconstructions, the SNR varied from 3.5 to 5.5, with probabilities of error from 10^{-5} to 10^{-7}.

There are two main reasons for the improvement in reconstruction quality with 633 nm as opposed to 488 nm. One reason is that the 633-nm reference beam was polarized in plane whereas the 488-nm reference was polarized out of plane. Hence the 633-nm reconstruction benefited from a higher diffraction efficiency. The second factor is the method used for averaging pixel values in the reconstructions: the program we used to calculate SNR averages the CCD pixels only within a margin of each image pixel; edge values are discarded. Hence any blurring effect at the edges of pixels in the x dimension becomes less of a factor for the SNR and the error calculations.

5. Erasure

We now examine how well the dual-wavelength architecture reduces the decay rate resulting from the readout illumination. We recorded two holograms with the same exposure at 488 nm and erased one with a non-Bragg-matched beam at 488 nm and the
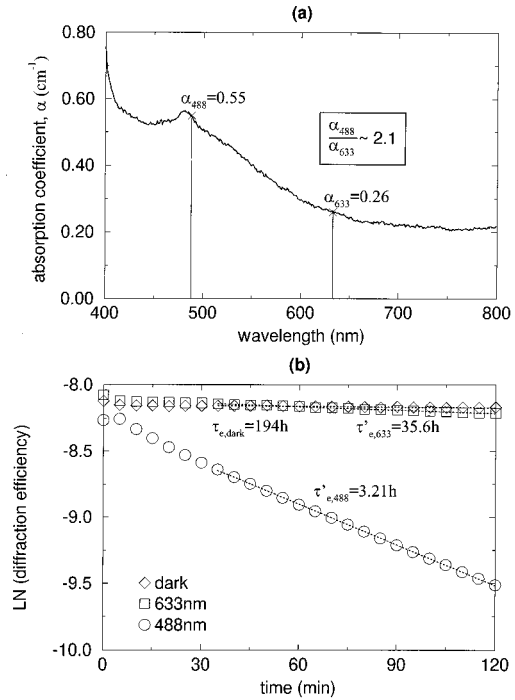
other with an equal intensity (21.4 mW/cm^2) beam at 633 nm, periodically monitoring the grating strength by probing with a 633-nm readout beam. The decay rate was also measured with no erasure beam to determine the decay contribution from dark conductivity as well as from the monitoring beam. The decay characteristics are plotted in Fig. 13(b). The measured erasure time constant (which includes the effects of dark erasure) for the 488-nm erasure was $\tau_{e,488}' = 3.21$ h, while that for the 633-nm erasure was $\tau_{e,633}' = 35.6$ h, giving a reduction in the readout decay rate by a factor of 11.1. However, after factoring out the dark decay ($\tau_{e,\mathrm{dark}} = 194$ h), modeling the overall decay as

$$\exp(-t/\tau_e') = \exp(-t/\tau_e)\exp(-t/\tau_{e,\mathrm{dark}}), \qquad (14)$$

where τ_e' is the measured erasure time constant including dark effects, τ_e is the erasure time constant resulting from the erasing illumination, and $\tau_{e,\mathrm{dark}}$ is the erasure time constant resulting from the dark conductivity and erasure from the monitoring beam, we find the actual contribution caused by the illumination to be $\tau_{e,488} = 3.27$ h and $\tau_{e,633} = 43.6$ h, corresponding to a ratio of 13.3.

The absorption spectrum for this crystal is shown in Fig. 13(a). For the two wavelengths used in our experiment, the absorption coefficients were $\alpha_{488} = 0.55$ cm^{-1} and $\alpha_{633} = 0.26$ cm^{-1}. The ratio of these coefficients is 2.1; therefore the ratio of 13.3 in erasure time constants was larger than expected. At this point we have not yet developed a theoretical model to predict relative erasure times from the ab-
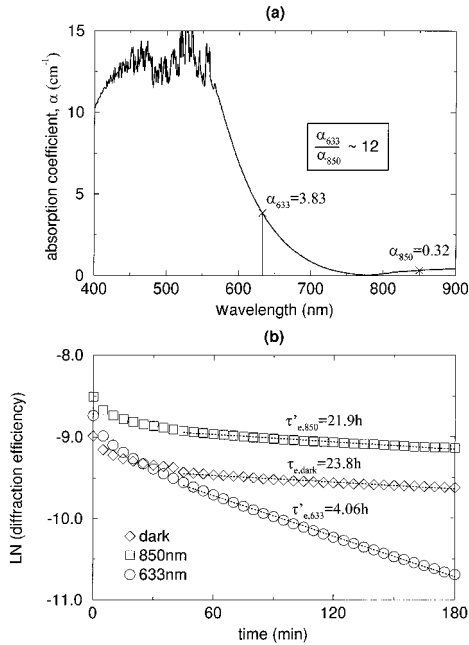
Fig. 14. (a) Absorption spectrum and (b) decay curves for the LiNbO$_3$:Fe:Ce crystal.

sorption spectrum. However, it should not be entirely surprising that the ratio of absorption coefficients is different from that of the erasure time constants because not every photon that is absorbed will contribute toward the erasure of the hologram. For example, some energy will be absorbed by the lattice, or an electron may be excited into the conduction band but immediately trapped again. Still, we expect that larger ratios in absorption coefficients will be reflected in larger ratios in erasure time constants.

One important note is that the choice of crystal and the wavelengths used in this experiment were not optimized for the dual-wavelength architecture but were based on the lasers available in the laboratory. The crystal was one that we have had good results with in the past, and 488 and 633 nm were laser wavelengths that were readily at hand with good power output. However, to maximize the benefits of the dual-wavelength scheme, we can certainly be more selective in our choice of crystal and system parameters.

For instance, Fig. 14(a) shows the absorption spectrum for a doubly doped LiNbO$_3$:Fe:Ce (0.05% Fe, 0.03% Ce) crystal from Deltronic (Deltronic Crystal Industries, Inc., Dover, N.J.) that we have also used in dual-wavelength experiments. This crystal exhibits a range of absorption coefficients over the same range of wavelengths that is much wider than the crystal that we used for the 1000-hologram experiment. We tested this crystal using $\lambda_1' = 633$ nm for recording and $\lambda_2' = 850$ nm for readout, corresponding to absorption coefficients of $\alpha_{633} = 3.83$ cm^{-1} and $\alpha_{850} = 0.32$ cm^{-1}, respectively. This gives a ratio of

12.0 of absorption coefficients, nearly 6 times that for the previous crystal and wavelengths.

Figure 14(b) shows the erasure characteristics that we measured for the two wavelengths with equal intensities of 15.7 mW/cm^2, as well as for the dark erasure. From the data we obtained the erasure time constants (including dark effects), $\tau_{e,633}' = 4.06$ h and $\tau_{e,805}' = 21.9$ h. Again, factoring out the dark erasure ($\tau_{e,\mathrm{dark}} = 23.8$ h) according to relation (14) to get the true decay contributions caused by the illumination, we get $\tau_{e,633} = 4.79$ h and $\tau_{e,850} = 273.4$ h, giving a reduction in the erasure rate by a factor of 57.1.

These results verify that we can reduce greatly the decay caused by the readout illumination by using a second wavelength at which the crystal is relatively insensitive. However, the results also illustrate a fundamental limitation of the dual-wavelength scheme, and that is the problem of dark erasure. Although we may factor out the dark decay in calculating the effectiveness of using two wavelengths, we cannot ignore it in practice and it will remain a limiting factor of this approach.

6. Storage Density

Previously we demonstrated the storage of 1000 holograms with the dual-wavelength architecture. Now we examine the theoretical limits of this method in terms of the potential storage density of an image-plane system. Because of the limitation on pixel size imposed by the dual-wavelength method, there will necessarily be a reduction in storage density compared with what could be achieved by the normal single-wavelength scheme (reading out the holograms with the original reference beam). The following analysis is a simplified version of that done by Li[15] for determining storage density.

Because we are dealing with transmission geometry, we use the surface storage density as the figure of merit. We can write the surface density D as

$$D = \frac{N_\phi N_\psi N_{px} N_{py}}{A}, \qquad (15)$$

where N_ϕ is the number of angular multiplexed locations; N_ψ is the number of peristrophic locations; N_{px} and N_{py} are the number of pixels in the x and y dimensions, respectively, in each hologram; and A is the surface area of the hologram.

For simplicity, we assume the signal beam to be normal to the crystal face and that angular multiplexing is achieved by tilting the angle of the reference beam instead of by rotating the crystal. This way we may treat the hologram area as constant for all multiplexing locations. Further, we take the hologram area to be that at the image plane inside the crystal, neglecting the defocusing effect of the signal beam away from the image plane. This is acceptable if we filter out the reconstructions from adjacent re-

cording locations at a subsequent image plane. We may then write the hologram area as

$$A = (N_{px}\delta_x)(N_{py}\delta_y), \qquad (16)$$

where δ_x and δ_y are the x and y dimensions of each pixel in the image. Equation (15) then becomes

$$D = \frac{N_\phi N_\psi}{\delta_x \delta_y}, \qquad (17)$$

which is simply the number of holograms that can be multiplexed at the same location divided by the area of one pixel.

The number of angular multiplexed locations we can access by tilting the reference beam is determined by the span of angles available for the reference and by the angular selectivity. If a rotating mirror and $4f$ system are used to tilt the reference beam, then the total angular range Φ is limited by the aperture of the lens and the beam width and is given by

$$\Phi = 2 \tan^{-1}\left(\frac{A - W}{2F}\right). \qquad (18)$$

W is the width of the reference beam, and A and F are the aperture and the focal length, respectively, of the $4f$ system. The angular selectivity $\Delta\phi$ in the dual-wavelength case is given by Eq. (9). If we record at the second null, the total number of angular multiplexed locations is then simply

$$N_\phi = \frac{\Phi}{2\Delta\phi}. \qquad (19)$$

Although we used peristrophic multiplexing in our 1000-hologram experiment, it is not a practical multiplexing method in a high-density storage system where small pixels must be used. For pixel sizes of the order of a few micrometers, the peristrophic selectivity will be of the order of tens of degrees. This is especially limiting when we record with photorefractive crystals in the transmission geometry because we are constrained to a relatively small range of angles that we can tilt the c axis while we still maintain acceptable recording efficiencies (refer to Fig. 7). Use of peristrophic multiplexing would gain us perhaps a factor of only 2–6 in density; hence we neglect it in this analysis.

The minimum pixel dimension we may use in the y dimension is determined by the resolution limit of the system optics according to the relation

$$\delta_y = \frac{\lambda_2'}{\sin\left[\tan^{-1}\left(\dfrac{1}{2(f\text{-number})}\right)\right]}. \qquad (20)$$

However, the x dimension is constrained by the minimum pixel width $\delta_{x,\min}$ of the dual-wavelength scheme, given by Eq. (7), which for $\theta_s = 0°$ becomes

$$\delta_x = L \tan \phi_s. \qquad (21)$$

Combining all terms, we obtain the final density equation:

$$D = \frac{\sin(\phi_s + \phi_r)}{\lambda_2' 2 \sin \phi_s} \tan^{-1}\left(\frac{A - W}{2F}\right)$$
$$\times \sin\left\{\tan^{-1}\left[\frac{1}{2(f\text{-number})}\right]\right\}. \qquad (22)$$

For example, with the parameters $\lambda_1' = 488$ nm, $\lambda_2' = 633$ nm, $\theta_s = 0°$, $\theta_r = 10°$, $W = 1$ cm, $A = 5$ cm, and $F = 5$ cm (f-number = 1), then $D = 3.7$ bits/μm². Note that this formula is independent of the crystal thickness L. Although we might improve the storage density of a single-wavelength system by increasing the crystal thickness (and thus reducing the angular selectivity), in the dual-wavelength case this increase in the number of angular multiplexing locations is cancelled by a corresponding increase in $\delta_{x,\min}$, which reduces the number of pixels per page. The density that can be achieved with the dual-wavelength scheme becomes comparable with that for one wavelength only if the crystal is thin or if the two wavelengths are close enough to each other so that $\delta_{x,\min}$ approaches δ_y (the resolution limit of the optics).

7. Conclusion

A dual-wavelength architecture can significantly reduce the decay of holograms resulting from readout. However, such an architecture does introduce new complexities and problems to the system, some of which we addressed here while others still require further investigation. On the system side, we have shown that we can minimize the Bragg-mismatch problem of the dual-wavelength scheme by properly adjusting system parameters, primarily the thickness of the crystal (something that can be done conveniently for a holographic three-dimensional disk). We also combine peristrophic with angle multiplexing to counter the poorer angular selectivity of thin crystals, while we adjust the recording schedule to compensate for the varying recording characteristics for different crystal tilts. Also, by recording holograms in the image plane, we can retrieve entire data pages at one time with a simple plane-wave readout beam, without the added complexity of spherical beams or interleaving holograms. We were thus able to record 1000 holograms and read them out with significantly reduced decay by using two wavelengths.

Two main problems remain, however. The first is the problem of dark conductivity. As was shown above, dark erasure can severely limit the effectiveness of the second wavelength at reducing the decay rate. Furthermore, the dark erasure prevents a dual-wavelength architecture from truly maintaining a constant grating strength, because at best it can only eliminate the decay caused by the readout process. In contrast, periodic copying, for example, can restore the strength of holograms regardless of the cause of the holographic decay—whether it is due to

readout or dark conductivity. Hence a dual-wavelength scheme will probably be most useful when it is used in conjunction with some other process, such as copying, so as to expand the time frame over which we can refresh the holograms. It might be possible to affect the dark conductivity by changing the crystal temperature, impurity dopants, or oxidation–reduction state.

The second problem is the density limitation. Because of the $\delta_{x,\min}$ constraint, the dual-wavelength system restricts the storage density of the system except where thin crystals are being used. Alternatively, if the crystal exhibits sharp changes in absorption behavior for small changes in wavelength, the density can approach that of the single-wavelength system. Otherwise the dual-wavelength system will be most useful for storing large numbers of holograms in a dynamic system in which high resolution is not a necessity.

References

1. J. J. Amodei and D. L. Staebler, "Holographic pattern fixing in electro-optic crystals," Appl. Phys. Lett. **18,** 540–542 (1971).
2. F. Micheron and G. Bismuth, "Electrical control of fixation and erasure of holographic patterns in ferroelectric materials," Appl. Phys. Lett. **20,** 79–81 (1972).
3. D. von der Linde, A. M. Glass, and K. F. Rodgers, "Multiphoton photorefractive processes for optical storage in LiNbO$_3$," Appl. Phys. Lett. **25,** 155–157 (1974).
4. D. Brady, K. Hsu, and D. Psaltis, "Periodically refreshed multiply exposed photorefractive holograms," Opt. Lett. **15,** 817–819 (1990).
5. H. Sasaki, Y. Fainman, J. E. Ford, Y. Taketomi, and S. Lee, "Dynamic photorefractive optical memory," Opt. Lett. **16,** 1874–1876 (1991).
6. S. Boj, G. Pauliat, and G. Roosen, "Dynamic holographic memory showing readout, refreshing, and updating capabilities," Opt. Lett. **17,** 438–440 (1992).
7. Y. Qiao and D. Psaltis, "Sampled dynamic holographic memory," Opt. Lett. **17,** 1376–1378 (1992).
8. H. Külich, "Reconstructing volume holograms without image field losses," Appl. Opt. **30,** 2850–2857 (1991).
9. R. McRuer, J. Wilde, L. Hesselink, and J. Goodman, "Two-wavelength photorefractive dynamic optical interconnect," Opt. Lett. **14,** 1174–1176 (1989).
10. D. Psaltis, F. Mok, and H. Li, "Nonvolatile storage in photorefractive crystals," Opt. Lett. **19,** 210–212 (1994).
11. K. Curtis, A. Pu, and D. Psaltis, "Method for holographic storage using peristrophic multiplexing," Opt. Lett. **19,** 993–994 (1994).
12. H. S. Li, "Photorefractive 3-D disks for optical data storage and artificial neural networks," Ph.D. dissertation (California Institute of Technology, Pasadena, Calif., 1994).
13. H. Li and D. Psaltis, "Double grating formation in anisotropic photorefractive crystals," J. Appl. Phys. **71,** 1394–1400 (1992).
14. D. Psaltis, D. Brady, and K. Wagner, "Adaptive optical networks using photorefractive crystals," Appl. Opt. **27,** 1752–1759 (1988).
15. H. Li and D. Psaltis, "Three-dimensional holographic disks," Appl. Opt. **33,** 3764–3774 (1994).